Adsorption performances of Methylene blue by poly(vinylidene fluoride)/ MWCNT membranes via ultrasound-assisted phase inversion method

Yangyang Huan[a], Zhipeng Li[a], Chunqing Li[b], Guangfen Li[a],*

[a]*State Key Laboratory of Separation Membranes and Membrane Processes, School of Materials Science and Engineering, Tianjin Polytechnic University, Tianjin 300387, China, Tel. +86 22 83955074; Fax: +86 22 83955055; email: liguangfen@tjpu.edu.cn*
[b]*School of Computer Science and Software Engineering, Tianjin Polytechnic University, Tianjin 300387, China*

ABSTRACT

In this study, poly(vinylidene fluoride) (PVDF)/MWCNT composite membranes were successfully prepared via an ultrasound-assisted phase inversion process. The influences of the ultrasonic power and ultrasonic time on the variation of membrane morphology, hydrophilicity, porosity and adsorption performances to methylene blue (MB) dye were comprehensively investigated. Scanning electron microscope analysis indicated that low ultrasonic power (60 W) and long ultrasonic time (60 s) are in favour of the formation of finger-like pores, causing super water flux, high porosity and large mean pore size of membranes. A maximum adsorption capacity of the ultrasound treated membrane reached up to 4.4 mg/g, which is higher than the untreated membrane (2.4 mg/g). Furthermore, the kinetics and isotherm models studies indicated that the adsorption of MB followed a pseudo-second-order kinetic model and Freundlich isotherm model.

Keywords: Poly(vinylidene fluoride); MWCNT; Ultrasound; Methylene blue; Adsorption properties

1. Introduction

As we all known, the rapid development of dye industries including cosmetics, textiles and food processing has caused serious harm to the environment through discarding colourful dye and partial deleterious organic materials in wastewater [1]. These industrial wastewater pollutants contain many kinds of dyes, which are difficult to remove and separate because of their complex composition. Therefore, the reuse of dye wastewater becomes a difficult problem [2]. There are many ways to remove dyes from wastewater, including adsorption [3], extraction [4], membrane separation [5], catalysis [6,7] and biological methods [8]. Among these methods, adsorption is considered to be one of the most ideal methods [9]. The adsorption method not only has high adsorption efficiency and low cost but also does not produce additional harmful substances [10,11].

Ultrafiltration (UF) membrane is extensively used in wastewater treatment due to its ability in filtering out proteins [12], colloids [13], viruses [14] and other particles present in water resources [15,16]. The commonly used UF membrane materials include poly (ethersulfone) (PES), poly (sulfone) (PSF) and poly(vinylidene fluoride) (PVDF). Among these membrane materials, PVDF has been regarded as one potential membrane material and thus has been widely utilized in ultrafiltration processes owing to its unique physical and chemical properties as its high thermal stability, high mechanical properties and good chemical resistance [17–19]. However, its hydrophobic characteristics and being easily contaminated during wastewater separation process cause the rapid decline of the water flux [19] and therefore restrict its application in different areas. To this problem, an incorporation of nanomaterials into the membrane

---

* Corresponding author.

matrix [20] was adopted. By incorporating different kinds of nanoparticles such as silica, graphite and carbon nanotubes (CNTs) into the membranes, mechanical properties, permeability and fouling resistance can be improved [21,22]. CNTs are ideal nano-fillers due to their excellent electrical conductivities, outstanding mechanical (stiffness and flexibility) and thermal properties [23,24], and their effective water treatment capabilities in dealing with organic contaminants [25,26]. As far as we know, dye adsorption by PVDF composite membranes as PVDF/graphene oxide nanohybrid membranes [27] and cellulose nanofibre-based PVDF membrane [28] has been found to be an effective way to remove dyes from wastewater due to its high economic efficiency and polymer-based membranes have the advantages of preparation simplicity and have attracted more attentions [29,30]. However, the studies on adsorption behaviour of polymer membranes were limited due to the low adsorption capacity in comparing with inorganic adsorbents. Therefore, it is an important research direction to explore composite membrane adsorbents with high adsorption capacity and good selectivity.

For the past few years, ultrasound has been widely used in water treatment with membrane by several researchers. Hou et al. [31] carried out a study to investigate the effect of ultrasonic irradiation on membrane scaling mitigation during membrane distillation process. Borea et al. [32] found that ultrasound can enhance wastewater treatment by membrane ultrafiltration and discussed the effect of ultrasonic frequency on membrane flux. Tao et al. [33] successfully prepared PVDF membranes by an ultrasound-assisted phase inversion method. An ultrasound is also confirmed to be a powerful way to polymerize and disperse nanoparticles and is also extensively used in modifying polymer surfaces [34]. Ultrasound can cause a series of physical phenomena and assist chemical reactions. When the liquid is exposed to radiation, the bubbles will generate turbulence, leading to strong high pressure and sound flow, which will change the surface structure and internal pore structure of the composite membrane. Therefore, the pore structure with excellent adsorption properties can be prepared by controlling the appropriate ultrasonic conditions to improve the adsorption efficiency [35]. To the best of our knowledge, even though ultrasound was increasingly applied to membrane preparation for wastewater treatments, the effects of ultrasonic power and ultrasonic time to the fabricated membranes were not investigated yet in the previous papers.

In this study, PVDF/MWCNT nanocomposite membranes were prepared by a solution casting method coupling with an ultrasound-assisted phase inversion. The effects of ultrasonic power and ultrasonic time on membrane morphology, surface hydrophilicity, material porosity, mechanical properties, water permeability and BSA rejection of the corresponding membranes were investigated. In addition,

we selected methylene blue (MB) for the adsorption experiment to study the adsorption performance of the composite membranes. The adsorption process of MB on composite membranes was analyzed by kinetics and isotherms. The morphology and chemical group analysis of the composite membranes before and after adsorption were carried out to speculate the adsorption mechanism.

2. Experimental

2.1. Materials

The PVDF powder was acquired from Dongguan Tengda plastic material Co. Ltd., (China) (M_w = 45,000). It was dried at 60°C in the oven for 5 h before using it. The carboxylated MWCNTs were obtained from Chengdu Organic Chemistry Research Institute (China). N,N-Dimethylformamide (DMF, ≥99.5%) was purchased from Tianjin Kermel Chemical Reagents Co. Ltd. (China), and bovine serum albumin (BSA, M_w = 68,000) was bought from Solarbio Science and Technology Co. Ltd., Beijing. Methylene blue (MB, M_w = 373.9, C.I. number: 52015) was purchased from Tianjin Guangfu Chemical Research Institute (China).

2.2. Preparation of PVDF/MWCNT membranes

Using the carboxylated MWCNTs with the weight of 1 wt.% of casting solution dispersed in 82 wt.% DMF and then irradiated in an ultrasonic instrument (KQ-300VDE, Kunshan, China). Moreover, weighted the PVDF powder with 17 wt.% of casting solution, added to the MWCNT/DMF mixed solution and stirred for 4 h at 70°C in a water bath to obtain a uniform solution, which was then placed in the vacuum drying oven for 12 h to remove the bubbles through the vacuum environment.

The casting solution is evenly spread onto the glass plate as a substrate and scraped into membranes by a casting knife with a thickness of 200 μm. Then, the scraped membrane was put into the ultrasonic instrument with deionized water for radiation to assist the phase inversion. The temperature of the coagulation bath remained at 26°C. Subsequently, the membranes were automatically detached from the substrate. Finally, these membranes were again placed in fresh deionized water for 12 h for the removal of DMF. As a result of the time of ultrasonic radiation being only tens of seconds, the thermal effect produced by the ultrasonic radiation was negligible. At last, the membrane was dried in an oven at the temperature of 50°C. The treatments for various membranes under selected ultrasonic conditions are then summarized in Table 1. Ten total samples are named by Mn with *n* varying from 0 to 9, respectively.

Table 1
Treatments for various membranes under selected ultrasonic conditions

Samples	M0	M1	M2	M3	M4	M5	M6	M7	M8	M9
Ultrasonic power (W)	0	60	60	60	80	80	80	100	100	100
Ultrasonic time (s)	0	20	40	60	20	40	60	20	40	60

2.3. Membrane characterization

2.3.1. Membrane morphology and hydrophilicity (contact angle measurement)

A scanning electron microscope (SEM, S-4800, Hitachi, Japan) was used for observing the morphology of the fabricated membranes. The membrane samples were broken in liquid nitrogen and sprayed with gold before observing.

The surface hydrophilicity of these membranes was performed by placing sessile droplets of deionized water on membrane surfaces and then measuring their contact angles using a goniometry instrument (DSA 100, KRUSS, Germany). The membrane samples were cut into 5 cm × 5 cm pieces and placed on a glass plate. The volume range of water droplets is 2 μL. Each group was measured 10 times and averaged.

2.3.2. Mechanical properties

The mechanical properties of the membranes were assessed at 25°C using a LLY-06, Laizhou Electron Instrument Co. Ltd., China. The dried membrane was cut into the shape of a rectangle with a length of 3 cm and wide of 0.5 cm. The tensile rate was set with 2 mm/min. Each sample was stretched three times, and the results were averaged.

2.3.3. Zeta potential

The surface charge property of a solid membrane was surveyed using the streaming potential method. The electrokinetic analyzer from SURPASS, Anton Paar (Austria) was used for this experiment. The zeta potential was calculated from the flow potential and pressure diagram using the Helmholtz–Smoluchowski equation [36]. The experiments were performed under pH values from 3 to 10 and an ionic strength of 0.001 mol/mL KCl at 25°C.

2.3.4. Membrane porosity and mean pore size

The porosity of membranes was obtained by the wet-dry method. The wet membrane was cut into a 5 cm × 5 cm square shape and then placed in a glass tray and dried in the oven. The mass of the wet and dry membrane samples was weighed. The porosity (ε) was measured by Eq. (1):

$$\varepsilon = \frac{\dfrac{\left(w_w - w_d\right)}{\rho_{\text{water}}}}{\dfrac{\left(w_w - w_d\right)}{\rho_{\text{water}}} + \dfrac{w_d}{\rho_p}} \tag{1}$$

where w_w and w_d are the weights of the wet membrane (g) and dry membrane (g), respectively, ρ_{water} is the density of pure water (0.998 g/cm³), and w_d/ρ_p is the volume of the membrane. The mean pore radius (r_m) was calculated according to Eq. (2):

$$r_m = \sqrt{\frac{(2.9 - 1.75\varepsilon) \times 8\mu l Q'}{\varepsilon \times A \times \text{TMP}}} \tag{2}$$

Here, Q' represents the volume of water permeability per second (m³/s), and μ and TMP are the water viscosity (8.9 × 10⁻⁴ Pa s) and trans-membrane pressure (Pa), respectively. l and A are the thickness (m) and the area of membrane (m²), respectively.

2.3.5. Membrane performance

The water flux and BSA rejection are the main performance measures of membranes, which can be characterized by a cross-flow system with an effective area of 22.9 cm², as shown in Fig. 1. The membrane in the water flux test system was pre-pressed under 0.3 MPa for 10 min to achieve a stable water flux. Then, the pure water permeability was assessed at 0.2 MPa and recorded every 10 min. The water permeation flux was calculated as in Eq. (3).

The BSA rejection experiment was carried out by using a 1 g/L BSA solution prepared by dissolving 1 g BSA in 1 L phosphate-buffered saline solution. The solution before and after the BSA rejection experiments were tested by UV–Vis spectrometry (UV-2401PC, Shimadzu, Japan) at 280 nm. The BSA rejection rate was calculated as in Eq. (4) [37]:

$$J = \frac{Q}{A \times T} \tag{3}$$

$$R = \left(1 - \frac{C_p}{C_f}\right) \times 100\% \tag{4}$$

where J represents the pure water flux of the membrane (L/m²/h), Q is the volume of water permeability (L) and T is the operated time (h). A is the effective area of the membrane sample (m²). R is the BSA rejection rate (%). The concentration of the BSA permeation and feed solution are C_p and C_f (g/L), respectively.
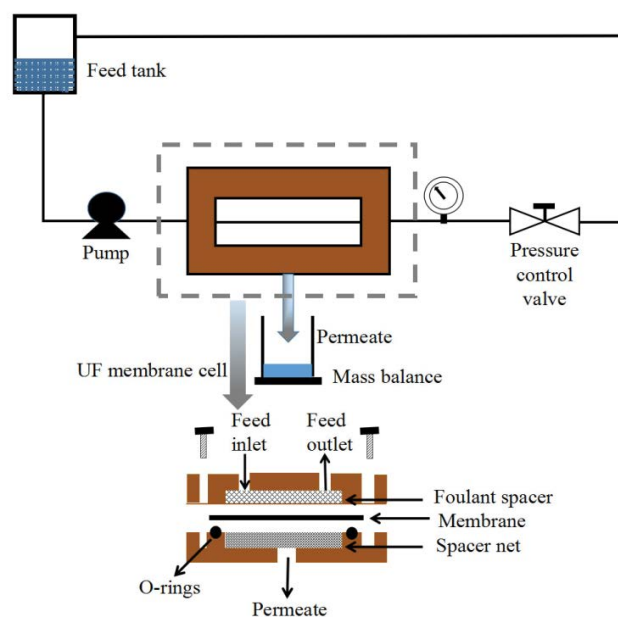
Fig. 1. Filtration performance of the prepared membranes was evaluated by a self-constructed cross flow system.

2.3.6. Membrane adsorption behaviour to methylene blue

We weighted 0.1 g of MB dye and dissolved it in 1 L deionized water to prepare the stock solution of 100 mg/L. The experimental solution was prepared by diluting the stock solution with deionized water to 10, 20, 30, 40 and 50 mg/L, respectively. In each adsorption experiment, the 30 mL samples of the MB solution were put in a 100 mL beaker, and then, the membrane sample was immersed in the dye solution. The adsorption capacity of MB with different concentration and time was measured for the kinetic and isotherm studies. The MB solution was surveyed at the wavelength of 663 nm by an UV-spectrophotometer (Shimadzu UV-2401PC, Japan). The membrane adsorption ability was calculated using Eq. (5) as follows:

$$q_e = \left(\frac{C_0 - C_e}{m} \right) \times V \tag{5}$$

where C_0 and C_e are initial and equilibrium concentrations of MB (mg/L), respectively, m is the mass of the adsorbent (g) and V is the volume of the solution (L).

By means of SEM, Fourier transforms infrared spectroscopy (FTIR, Nicolet, Thermo Fisher Scientific, USA) and the Brunauer, Emmett and Teller (BET, NOVA4200e, Anton Pacanta, USA) equation analysis of the composite membrane before and after adsorption, the adsorption mechanism of MB on the composite membrane was further proposed.

3. Results and discussion

3.1. Membrane morphologies

The SEM images of the cross sections (M0-a–M9-a) and the top surface (M0-b–M9-b) of the fabricated membranes with the variation of the ultrasonic power and time are exhibited in Fig. 2. All the membranes have the typical structure of the ultrafiltration membrane, namely, the dense top layer and the porous sublayer. Compared with the untreated PVDF membranes (M0-a and M0-b), the modified PVDF membranes with ultrasonic treatment exhibited a larger pore size in their surfaces and finger-like pores. The M1–M3 membranes have obvious macrovoids in their sublayers.

The cross-sectional morphologies of the membranes treated with low ultrasonic power (60 W) show that the macrovoid formations were prevented, and the finger-like pores had a good interconnection through cross-section. This indicates that the low ultrasonic power was propitious to the formation of longer finger-like pores with fewer macrovoids in the sublayer. However, with the increasing ultrasonic power, the finger-like pores of membranes begin to change to tear-drop-like voids. As the ultrasonic power was increased to 100 W, all of the finger-like pores transformed into tear-drop-like voids and equally distributed through the membrane cross-sectional area, as shown in Fig. 2 M7-a–M9-a.

For the membranes fabricated with ultrasonic irradiation of 60 W, such as M1-a, M2-a and M3-a, the finger-like pores ran through from the upper surface nearly to the bottom surface. Due to the turbulence of the ultrasound, the interface barrier between the finger-like pores and the underlying macropores was cleared up, resulting in the formation of long finger-like pores [33]. It is generally known that an ultrasound can promote the movement of molecules, and thus, it can also improve the diffusion speed of DMF. On one hand, ultrasonic radiation can aggravate the formation of finger-like pores by increasing the diffusion rate of water. On the other hand, with the increase of the ultrasonic power, the turbulence of liquid increases, which affects the rapid outflow of DMF, thus leading to the formation of tear-drop voids.

However, the diffusion speed of water is influenced by both the ultrasonic power and the hydrogen bonding between DMF and water. It was noted by Petersen that the interaction between hydrogen bonds between carbonyl oxygen and water molecules was stronger than that between hydrogen bonds between water molecules [38]. When the ultrasonic power was increased to 100 W, the DMF outflow was faster and the water inflow was slower, which led to more PVDF concentrated on the membrane in the process of phase inversion; subsequently, tear-drop-like voids and compressed cavities simultaneously appeared. As a result, higher ultrasonic power (100 W) leads to the formation of the cross-section structure with tear-drop-like voids.

The surface morphology of the corresponding membranes is presented in Fig. 2 M0-b–M9-b. It is expected that the ultrasonic irradiation leads to the formation of more pores. The M0–M3 membranes exhibit a relatively dense top surface. In contrast, the top surface of the membranes fabricated with higher ultrasonic irradiation exhibit a porous morphology. The ultrasonic cavitation is the main element, which produces higher energy phenomena and causes membrane surface damage. The impacts of the shock waves and micro jets on the surface will cause partial erosion. Along with the increase of the ultrasonic power, the damage of the membrane surface becomes more serious and results in the appearance of an entirely porous surface, as shown in Fig. 2 M7b, M8-b and M9-b.

3.2. Membrane hydrophilicity measurement

The hydrophilicity of all membranes treated with and without ultrasonication was evaluated by the water contact angle (CA), as shown in Fig. 3a. The CA for all ultrasonic-treated membranes maintains the same status below approximately 85°, which is obviously lower than the contact angle of the membrane M0 (87.2°). Moreover, the CA for the membranes treated with higher ultrasonic power was significantly lower than that treated with lower ultrasonic power. The lowest CA as 78.6° was found for the membrane M9, which was treated with highest ultrasonic power 100 W and longest ultrasonic time 60 s. The result is also consistent with the surface morphologies displayed in Fig. 2. Apparently, the tendency of the surface heterogeneity of the fabricated membranes increasing with ultrasonic power eventually dominates the surface hydrophilicity.

3.3. Porosity and mean pore size

The influences of the ultrasonic treatment on the porosity and pore size of the prepared membranes are shown in Fig. 3b. The porosity of all membranes is within the range
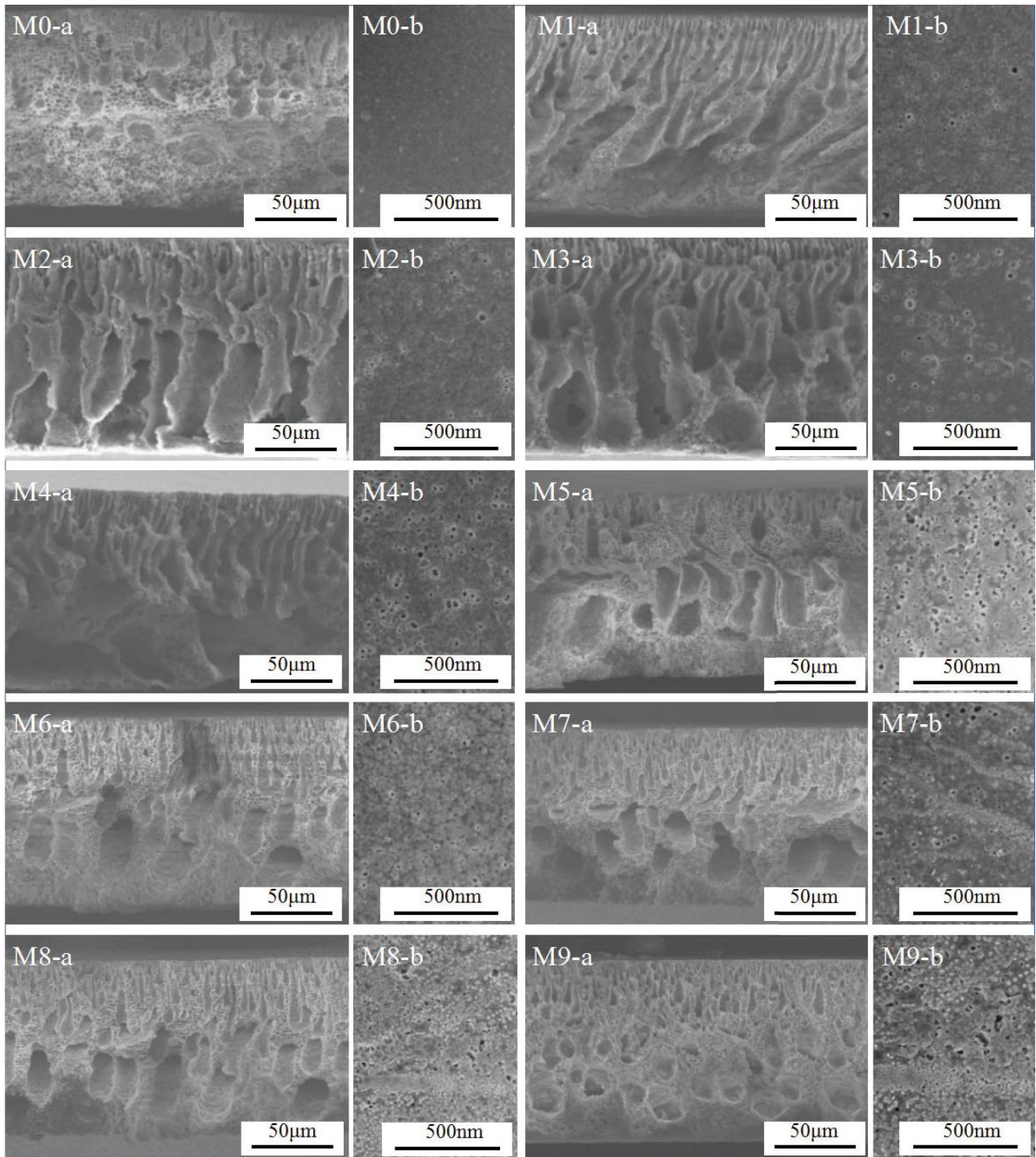
Fig. 2. SEM images of the cross sections (M1-a–M9-a) and the surfaces (M1-b–M9-b) of the fabricated membranes.

from 35% to 55%, whereas the mean pore size is within the range from 17 to 33 nm. The membrane M0 has the lowest mean pore size of 17.5 nm. With the variation of the ultrasonic conditions, the porosity and mean pore size of the ultrasonic-treated membranes have the coincident changes. Compared with the untreated membrane M0, the

ultrasonic-treated membranes contain larger pore size and higher porosity. A maximum value of the porosity as 55.8% was found for the membrane M3, which was treated with the ultrasonic intensity of 60 W. The porosity is then reduced as the ultrasonic intensity further increased to 80 and 100 W. A similar effect can also be found in the changes of the mean
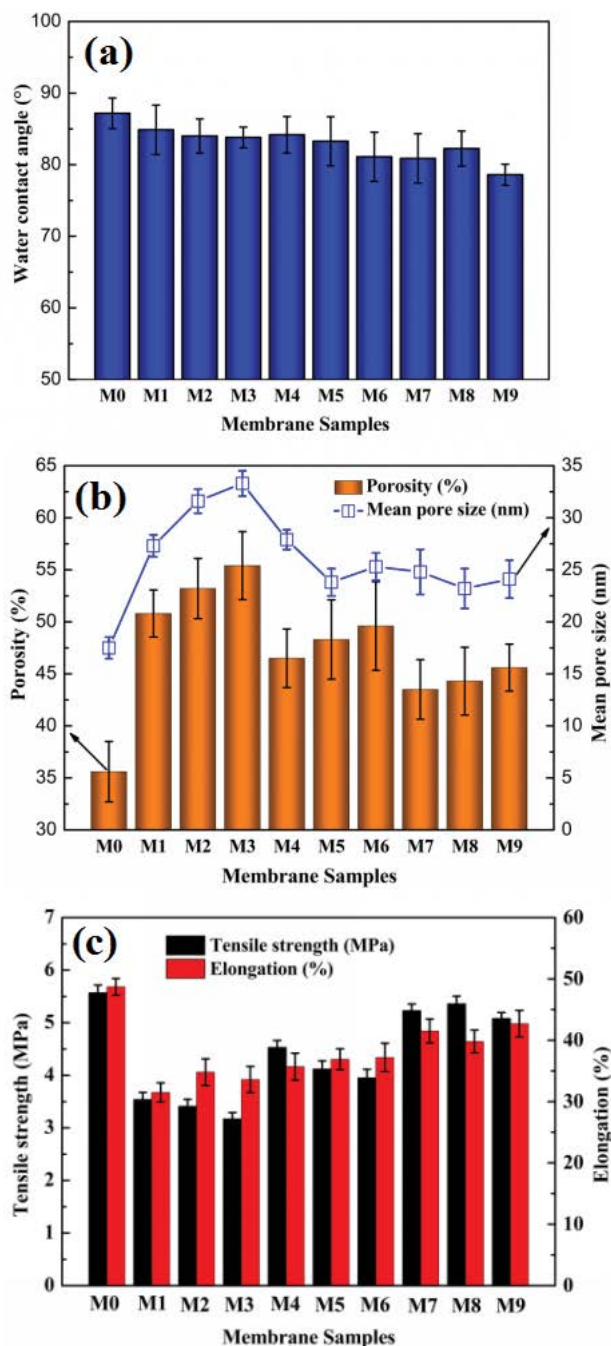
Fig. 3. (a) Water contact angles for all of the membrane samples, (b) porosity and mean pore size for all membrane samples, and (c) mechanical properties of tensile strength and elongation at the break of all membrane samples.

pore size. However, the mean pore size of the membranes M1–M3 fabricated with a lower ultrasonic intensity of 60 W is higher than the others. This is probably due to the structural variations in cross section of these membranes from dense to finger-like structures and then to macrovoids. Conclusively, the preferential ultrasound intensity can possibly result in an increase in both the pore size and the porosity of the corresponding membranes.

The extended ultrasonic time (20–60 s) will tend to slightly increase the porosity of the modified membranes and the mean pore size, as displayed in Fig. 3b. A clear view of the effects of the ultrasonic time (20–60 s) and ultrasonic power (60–100 W) to the porosity of the modified membranes are further plotted in Fig. 4a and b. It can be found that the membranes treated with the ultrasonic time of 60 s have higher porosities than the membranes with shorter ultrasonic times (Fig. 4a). In contrast, a low ultrasonic power (60 W) was more sufficient to increase the porosity of membranes than a high ultrasonic power (80 and 100 W), as shown in Fig. 4b. As we all know, the molecule movement can be improved by ultrasounds, thus leading to the increasing of the diffusion rate of DMF. However, unexpectedly, the ultrasonic power with 100 W cannot further expedite water diffusion.

3.4. PVDF/MWCNT mechanical properties

The mechanical properties of the corresponding membranes were tested and the results are summarized in Fig. 3c. All of the ultrasonic-treated membrane samples exhibited lower tensile strength compared with the untreated membrane. With the increase of the ultrasonic power, the tensile strength also decreased (5.57 MPa for the untreated membrane compared with a minimum value of 3.17 MPa for the membrane of M3). Since the tensile strength is related to the morphological structures and the porosity of membrane samples, it is dramatically affected by the ultrasonic conditions used. Similarly, Tao et al. have shown that the membranes with ultrasonic treatment exhibited lower tensile strength than the untreated membrane [33].

The tensile strength and elongation of the membranes fabricated with high ultrasonic power was apparently stronger than the membranes fabricated with low ultrasonic power. That is due to M1, M2 and M3 having enough finger-like pores running through the membrane section from the top surface to the bottom, as well as their higher porosity. At the same time, the membranes fabricated with high ultrasonic power have lower porosity and small tear-drop-like voids. Therefore, their tensile strength and elongation were superior to the membranes fabricated with low ultrasonic power.

3.5. Membrane performance

For evaluating membrane performance, experiments on pure water permeability and BSA rejection for all ultrasonic-treated PVDF/MWCNT membranes in comparison with the untreated PVDF membrane were carried out and the results are shown in Fig. 5. The water permeabilities of M1, M2 and M3 are superior to those of M4–M9, as shown in Fig. 5a. The stable water flux of M2 and M3 reaches 126 and 135 L/m²/h, respectively. This is due to that M2 and M3 have much more interconnected finger-like pores and dense porous structures near the bottom area. However, the membranes fabricated with high ultrasonic power contain more macrovoids and lower porosity, which results in a decrease of the water flux. The effect of increasing the membrane pore size and porosity would result in the increase of the water flux in accordance with the Hagen–Poiseuille equation [39]. Moreover, the untreated PVDF exhibited the lowest pure water flux of 75 L/m²/h because it has the highest hydrophobicity
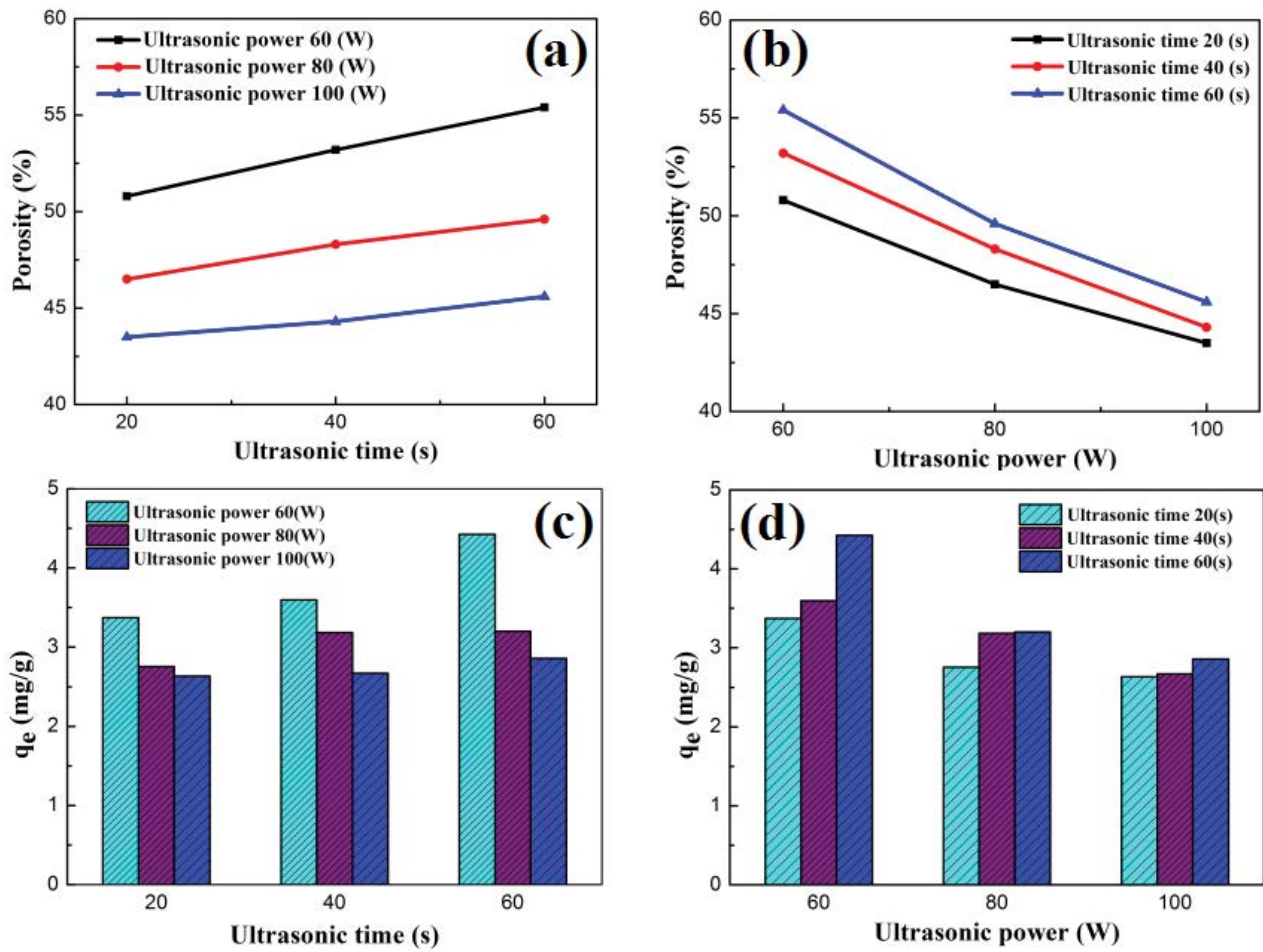
Fig. 4. (a) Effects of the ultrasonic time on the porosity of all membrane samples, (b) Effects of the ultrasonic power on the porosity of all membrane samples, (c) Effects of ultrasonic time (from 20, 40 to 60 s), and (d) ultrasonic power (from 60, 80 and 100 W) on the adsorption of MB for all ultrasonic-treated membranes.
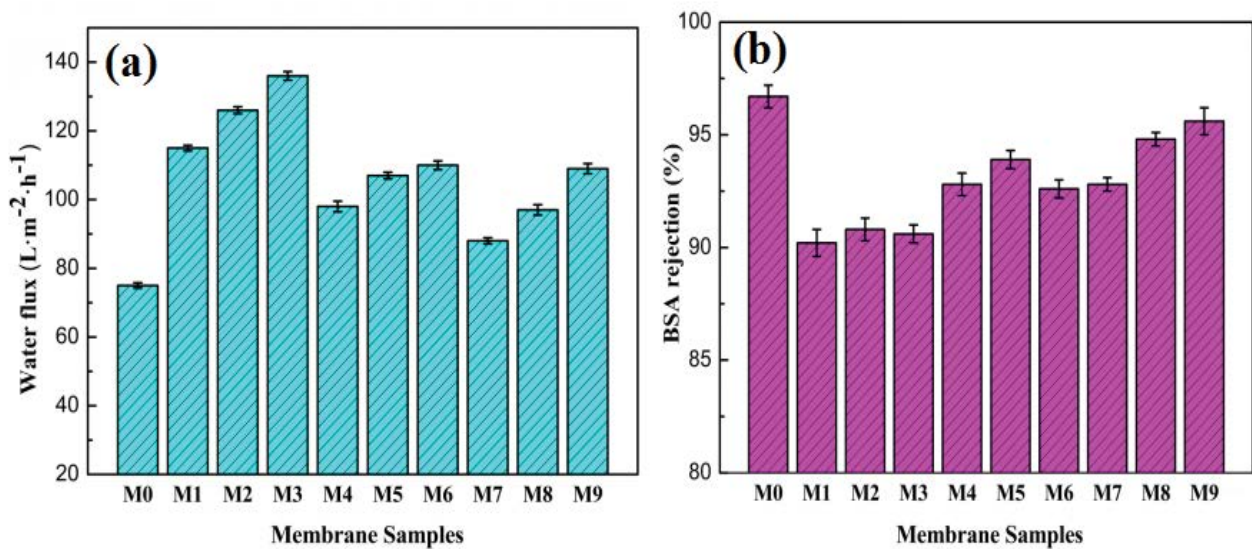
Fig. 5. (a) Pure water flux and (b) BSA rejection for all ultrasonic-treated PVDF/MWCNT membranes in comparison with the untreated PVDF membrane.

among all the membranes. Commonly, water permeability is determined by several effects, such as the chemical components, porosity, surface morphology, hydrophilicity, etc. In this case, the combined effects of surface hydrophilicity and porosity become major factors in dominating the membrane permeability.

The results of the BSA rejection rate are illustrated in Fig. 5b. It is well known that it is hard to balance the membrane flux and rejection. Despite the higher water flux found in ultrasound treated membranes, the BSA rejections of all the fabricated membranes with ultrasonic treatment were lower than the untreated membrane (96.7%). However, the BSA rejection rate of each membrane was still higher than 90%, which is because of the micro-sized pores and higher porosity in the modified membranes. In theory, due to the sieving mechanism, the ultrafiltration membrane has the ability of retention. Furthermore, the pore size of the membrane and the molecular size of the solute relatively influence the ability of membrane retention. In this study, all the surfaces of membrane samples contain almost dense structures (as exhibited in Fig. 2 M0-b–M9-b), which is the most important factor for the high rejection of BSA.

3.6. Adsorption capacity of methylene blue by membranes

3.6.1. Adsorption kinetics of membrane

For investigating the contact time dependence of the methylene blue adsorption properties by 10 different membranes, batch adsorption experiments were carried out under the same dye concentration of 30 mg/L. The plots of the adsorption capacity of methylene blue, q_e, as a function of the time are shown in Fig. 6. As a result of the adsorption of the molecules on the external surfaces of the membranes, the adsorption rate of all membranes had a rapid increase at first. The coming stage changed to a slow adsorption process. This shift is due to the MB molecules spreading into the inner porous structure of the membranes slowly. Furthermore, many of the available external adsorption sites were occupied at first.

It is obvious that all the q_e of the membranes fabricated with the ultrasonic treatment were higher than the q_e of the untreated membrane (M0). As a result, it can be concluded that the ultrasonic treatment of the membrane can improve the adsorption properties of the membrane to MB. As shown in Fig. 6a, the equilibrium adsorption capacity of MB on the untreated membrane (M0) was approximately 2.4 mg/g. Furthermore, for the M3 fabricated under the ultrasound power of 60 W and the time of 60 s, the adsorption process was quick to achieve the equilibrium state with a higher adsorption quantity, and it was increased to 4.4 mg/g with the same adsorption conditions. Then, M2 and M1 had the second and the third highest adsorption quantities of MB, respectively. This is due to their higher porosity caused by the ultrasonic treatment. By comparing the adsorption properties of different adsorbents to MB in Table 2, it can be seen that PVDF/MWCNT membrane has better adsorption properties for MB at low concentration.

Based on the optimized results of M3, the isotherm studies were carried out by immersing samples of M3 in different MB concentrations. As shown in Fig. 6b, the equilibrium adsorption quantity q_e raised with the increasing of the MB solution concentration. As the concentration of methylene blue dye solution is 50 mg/L, the equilibrium adsorption quantity q_e reaches the maximum, which is 5.68 mg/g.

Actually, the MB adsorption properties mechanism mainly rely on the factors of material porosity and surface potential [44,45]. Therefore, it is necessary to assess how the surface potential may affect the adsorption of MB using the membrane materials. The zeta potential is commonly applied to characterize the surface charge of the membranes. Here, three representative fabricated membranes with different adsorption performances were chosen to measure their zeta potential, as shown in Fig. 7. As expected, the zeta potentials of M1, M4 and M7 have almost the same potential between the pH values 3 and 10, which indicates that the ultrasonic treatment to the membrane will not change the zeta potential of the membrane. Thus, it can be concluded that the porosity and mean pore size of the membranes in this case are the most important factors in the MB adsorption
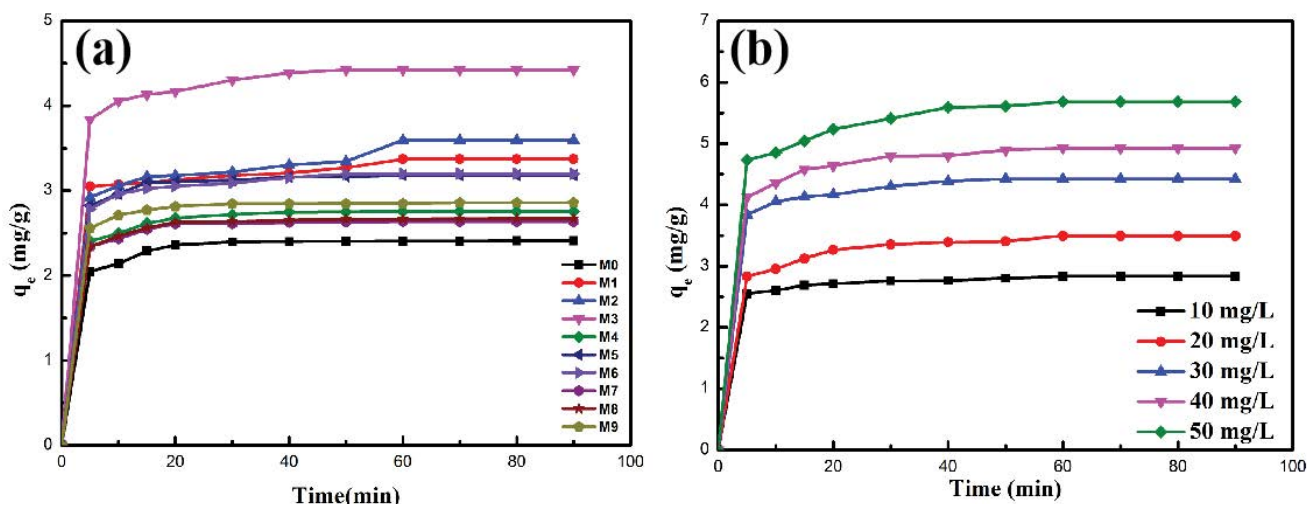
Fig. 6. Effects of contact time (a) and different concentration (b) on MB adsorption capacity by membrane samples.

Table 2
Comparison of PVDF/MWCNT membrane and other adsorbents for MB dye monolayer adsorption capacity

Adsorbent	Adsorption capacity (mg/g)	C_0 (mg/L)	Reference
Activated lignin–chitosan composite extrudates	36.3	82	[40]
Propylene diamine basic activated carbons	182.0	700	[41]
PVDF-ZnS pellets	0.5	30	[42]
NH_2-MWCNTs@Fe_3O_4	110.0	10	[43]
PVDF/MWCNT membrane	4.4	30	This work

performances. The characterization of zeta potential revealed that the surface of membrane in alkaline solution is negative charged (about –40 mV). When the membrane sample was placed in the MB solution, the methylene blue molecule will be adsorbed on the adsorption sites of the membrane surface due to the positive and negative charge attraction. The adsorption behaviour of the membrane samples in removing of a cationic dye as MB from aqueous solution is basically due to electrostatic interaction.

Fig. 4c and d show the influence of the ultrasonic time (20 s–60 s) and ultrasonic power (60–100 W) on the adsorption properties of the membranes to methylene blue dye. Fig. 4c shows that the maximum adsorption of the membranes fabricated with different ultrasonic times follows the order of 60 s > 40 s > 20 s. It can be seen that a longer ultrasonic time is beneficial to improve the adsorption performance of the membrane. However, in contrast, as Fig. 4d shows, the maximum adsorption of the membranes fabricated with different ultrasonic powers follows an order of 60 W > 80 W > 100 W. Higher ultrasonic power cannot improve the adsorption performance of the membrane. The results are consistent with the study of porosity and mean pore size for these membranes, as shown in Fig. 4a and b. The membrane fabricated with the lower ultrasonic power of 60 W possesses higher porosity and thus higher adsorption capacities.

3.6.2. Adsorption kinetic and isotherm models

Among all membranes, including the untreated membrane and the membranes fabricated under ultrasonic treatment, the M3 membrane has the best performance in all aspects. For further study of the adsorption process of methylene blue, experimental data based on M3 were fitted by two typical adsorption kinetic models, namely, the pseudo-first-order model and the pseudo-second-order model, as shown in Eqs. (6) and (7), respectively. The detailed information can be found in the related reference [46]. The value of these parameters and the correlation coefficient (R^2) are listed in Table 3.

$$\log\left(q_e - q_t\right) = \log q_e - \frac{k_1}{2.303}t \tag{6}$$

$$\frac{t}{q_1} = \frac{1}{k_2 q_e^2} + \frac{t}{q_e} \tag{7}$$
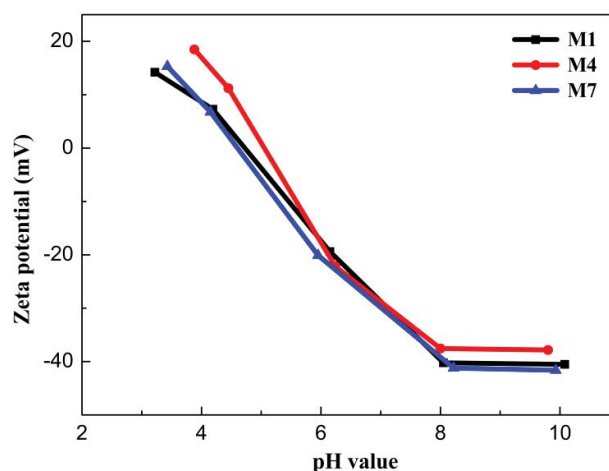
Fig. 7. Zeta potentials of various membranes.

Table 3 shows that the correlated coefficient (R^2) from the pseudo-second-order model is 0.998, which is higher than the pseudo-first-order model (0.990). Moreover, the results revealed that the adsorption data were more consistent with the pseudo-second-order model than the pseudo-first-order model (as shown in Fig. 8a), which indicates that the pseudo-second-order model is more suitable for the adsorption process. The reaction rapidly increased at first and then slowly decreased, which can be due to the decline of the available adsorbent sites and the concentration of MB dye [47].

The understanding of sample M3 adsorption isotherms was achieved by fitting the experimental data in two common models of Langmuir and Freundlich isotherm models, as shown in Eqs. (8) and (9). The value of these parameters and the correlation coefficient (R^2) are listed in Table 4.

$$\frac{C_e}{q_e} = \frac{1}{q_m K_L} + \frac{1}{q_m}C_e \tag{8}$$

$$\ln q_e = \ln K_F + \frac{1}{n}\ln C_e \tag{9}$$

where q_e (mg/g) is the equilibrium adsorption amount; C_e (mg/L) is the concentration of MB at equilibrium; q_m is the theoretical saturation capacity of the monolayer; K_L (L/mg) and K_F [(mg/g) (L/mg)$^{1/n}$] are the correlation indices of the

Table 3
Data of the pseudo-first-order and pseudo-second-order models

	Parameters	Value
Pseudo-first-order	$q_{e,cal}$ (mg/g)	4.331
	k_1 (min^{-1})	0.411
	R^2	0.990
Pseudo-second-order	$q_{e,cal}$ (mg/g)	4.457
	k_2 (g/mg/min)	0.248
	R^2	0.998

Table 4
Data of adsorption isotherms for the Langmuir and Freundlich models for the adsorption on M3 membrane

Isotherms	Parameters	Value
Langmuir	q_m (mg/g)	12.09
	K_L (L/mg)	0.029
	R^2	0.983
Freundlich	K_F [(mg/g) (L/mg)$^{1/n}$]	0.625
	n	1.547
	R^2	0.992

Langmuir isotherm and the Freundlich isotherm, respectively; n is the model reaction constant.

Table 4 shows that the R^2 by fitting the experimental data with Langmuir and Freundlich models were 0.983 and 0.992, respectively. Apparently, the fitting coefficient of the Freundlich model is higher than that of Langmuir model, suggesting the adsorption process of membrnae M3 on MB molecules is more consistent with latter model (as shown in Fig. 8b). The Langmuir isotherm assumes that the adsorption is a single layer of coverage and there is no interaction between the MB molecules [48,49]. Freundlich isotherms can be used for adsorption on non-uniform surfaces, typically for multilayer adsorption [50–52]. This indicates that the adsorption process is multilayer adsorption due to the pore structure of the membrane surface and the interaction between the membrane and dyes.

3.6.3. Adsorption mechanisms

Fig. 9 shows SEM images and an FTIR spectrum before and after adsorption of the composite membrane to MB. It can be seen from Fig. 9a and b that there are a lot of impurities in the pore of the composite membrane after adsorption compared with that before adsorption, which are formed by the aggregation of MB molecules. This is because there are innumerable interconnected pore structures in the composite membrane, and there is an adsorption field between them. MB molecules are absorbed into the pore and concentrated in the membrane pore under the force field. These forces include π–π conjugation effect, electrostatic attraction and hydrogen bonding. The interaction of π-electrons between the six-member ring of CNTs in the composite membrane and the aromatic ring structure of methylene blue produces the π–π conjugation effect. Zeta potential analysis showed that when the pH value exceeded 5, the surface of the composite film was negatively charged due to the presence of –OH, –COOH. The pH of the methylene blue dye (30 mg/L) used in the experiment was about 7, thus, the surface of composite membrane has a lot of negative charges. MB is a cationic dye that moves toward the surface of the composite membrane by electrostatic attraction. In addition, oxygen atoms in –OH and –COOH interact with hydrogen atoms in the MB molecule to form hydrogen bonds, further promoting the adsorption of the dye by the composite membrane.

In the infrared spectrum of Fig. 9c, the peak at 2,922 cm^{-1} corresponds to the stretching vibration of –C–H bond on methyl. The peaks at 761 and 612 cm^{-1} are assigned to the –C–H bond bending vibration peak. The peaks at 1,603 and
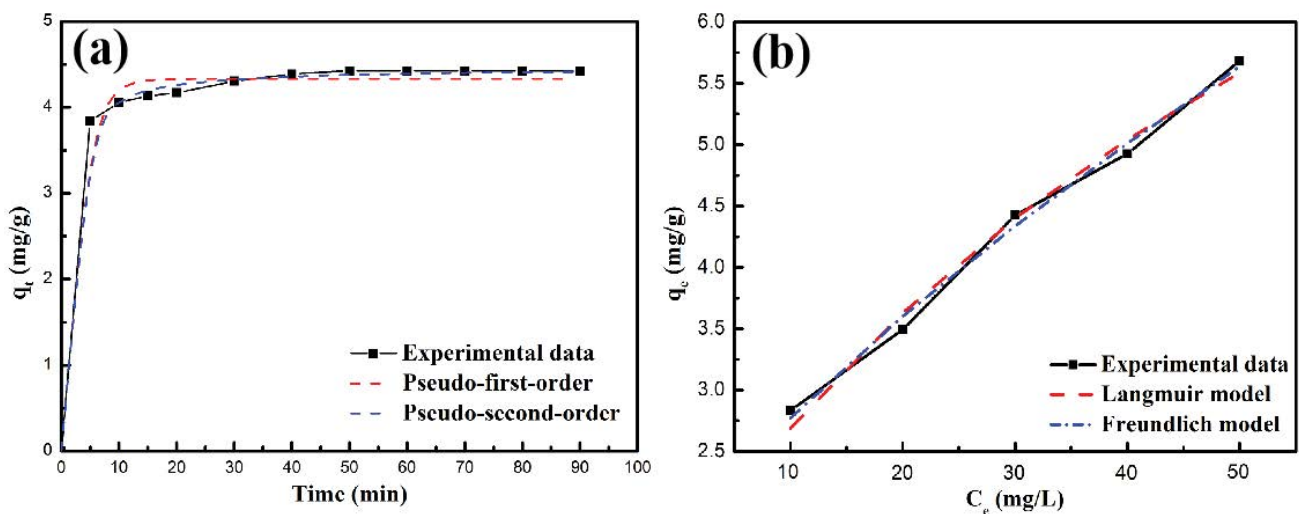
Fig. 8. Adsorption kinetic models of ultrasonic-treated membrane M3 (a) and adsorption isotherms of MB by membrane M3 at initial MB concentrations from 10 to 50 mg/L (b).
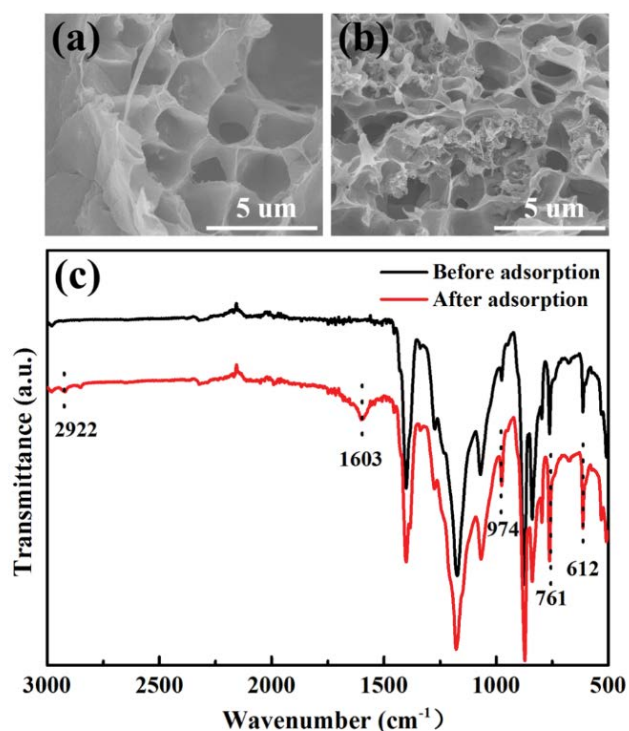
Fig. 9. SEM images of the composite membrane before (a) and after (b) adsorption and the FTIR (c) of the composite membrane before and after adsorption of MB.

Table 5
BET test parameters before and after adsorption of the composite membrane

Simple	Surface area (m^2/g)	Pore volume (cm^3/g)	N_2 adsorptive volume (cm^3/g)
Before adsorption	6.29	0.015	10.39
After adsorption	4.71	0.011	7.75

974 cm^{-1} are the skeleton vibration peaks of benzene ring and the –C–S bond vibration peaks, respectively. Compared with membrane before MB adsorption, it can be found that the peak intensity at these two positions after adsorption shows a significant change, indicating that the MB is strongly adsorbed by various forces. It was further verified by the changes of the BET test parameters before and after the adsorption of the composite membrane shown in Table 5. Clearly, MB was firmly adsorbed on the surface of the membrane and inside the pores. The aggregation of MB molecules causes the blockage of some pore structures, which results in the decrease of specific surface area, N_2 adsorptive volume and pore volume.

4. Conclusions

Ultrasonic irradiation during the phase inversion process had a great effect on the morphologies of PVDF membranes.

By increasing the ultrasonic power, the morphology of fabricated membranes changed dramatically from the original dense skin to regular large finger-like pores and then to teardrop-like voids. Both the porosity and the maximum adsorption of the membranes fabricated with different ultrasonic times follow an order of 20 s < 40 s < 60 s. Furthermore, both the porosity and the maximum adsorption of the membranes fabricated with different ultrasonic powers follow an order of 60 W > 80 W > 100 W. Moreover, all the performances for the water permeability of the fabricated membranes with the ultrasonic treatment were improved. The permeability and tensile strength mainly depended on the morphological variation. In addition, the kinetic studies show that the experimental data can be well fitted by the pseudo-second-order rate equation and more consistent with the Freundlich model. Through SEM, FTIR and BET analysis of the composite membrane after adsorption, it can be concluded that the adsorption of the composite membrane on methylene blue is due to the combined action of a variety of forces.

References

[1] M. Naushad, Z. Abdullah Alothman, M. Rabiul Awual, S.M. Alfadul, T. Ahamad, Adsorption of rose Bengal dye from aqueous solution by amberlite Ira-938 resin: kinetics, isotherms, and thermodynamic studies, Desal. Wat. Treat., 57 (2015) 13527–13533.
[2] H. Javadian, M.T. Angaji, M. Naushad, Synthesis and characterization of polyaniline/γ-alumina nanocomposite: a comparative study for the adsorption of three different anionic dyes, J. Ind. Eng. Chem., 20 (2014) 3890–3900.
[3] G.D. Sheng, D.D. Shao, X.M. Ren, X.Q. Wang, J.X. Li, Y.X. Chen, X.K. Wang, Kinetics and thermodynamics of adsorption of ionizable aromatic compounds from aqueous solutions by as-prepared and oxidized multiwalled carbon nanotubes, J. Hazard. Mater., 178 (2010) 505–16.
[4] N. Othman, R.N. Raja Sulaiman, H.A. Rahman, N.F.M. Noah, N. Jusoh, M. Idroas, Simultaneous extraction and enrichment of reactive dye using green emulsion liquid membrane system, Environ. Technol., 40 (2019) 1476–1484.
[5] X. Zhang, H. Li, J. Wang, D. Peng, J. Liu, Y. Zhang, In-situ grown covalent organic framework nanosheets on graphene for membrane-based dye/salt separation, J. Membr. Sci., 581 (2019) 321–330.
[6] M.G. da Rocha, S. Nakagaki, G.M. Ucoski, F. Wypych, G. Sippel Machado, Comparison between catalytic activities of two zinc layered hydroxide salts in brilliant green organic dye bleaching, J. Colloid Interf. Sci., 541 (2019) 425–433.
[7] X. Tao, Y. Han, C. Sun, L. Huang, D. Xu, Plasma modification of NiAlCe–LDH as improved photocatalyst for organic dye wastewater degradation, Appl. Clay Sci., 172 (2019) 75–79.
[8] G.G. Sonai, S.M. de Souza, D. de Oliveira, A.A. de Souza, The application of textile sludge adsorbents for the removal of Reactive Red 2 dye, J. Environ. Manage., 168 (2016) 149–156.
[9] G. Sharma, M. Naushad, A. Kumar, S. Rana, S. Sharma, A. Bhatnagar, F.J. Stadler, A.A. Ghfar, M.R. Khan, Efficient removal of coomassie brilliant blue R-250 dye using starch/poly(alginic acid-cl-acrylamide) nanohydrogel, Process Saf. Environ. Protect., 109 (2017) 301–310.

[10] M.M. Ayad, A.A. El-Nasr, J. Stejskal, Kinetics and isotherm studies of methylene blue adsorption onto polyaniline nanotubes base/silica composite, J. Ind. Eng. Chem., 18 (2012) 1964–1969.

[11] A.L. Cazetta, A.M.M. Vargas, E.M. Nogami, M.H. Kunita, M.R. Guilherme, A.C. Martins, T.L. Silva, J.C.G. Moraes, V.C. Almeida, NaOH-activated carbon of high surface area produced from coconut shell: kinetics and equilibrium studies from the methylene blue adsorption, Chem. Eng. J., 174 (2011) 117–125.

[12] K. Narsaiah, G.P. Agarwal, Transmission analysis in ultrafiltration of ternary protein mixture through a hydrophilic membrane, J. Membr. Sci., 287 (2007) 9–18.

[13] M. Dai, K.O. Buesseler, P. Ripple, J. Andrews, R.A. Belastock, Ö. Gustafsson, S.B. Moran, Evaluation of two cross-flow ultrafiltration membranes for isolating marine organic colloids, Mar. Chem., 62 (1998) 117–136.

[14] R. Lu, C. Zhang, M. Piatkovsky, M. Ulbricht, M. Herzberg, T.H. Nguyen, Improvement of virus removal using ultrafiltration membranes modified with grafted zwitterionic polymer hydrogels, Water Res., 116 (2017) 86–94.

[15] A. Vijayalakshmi, D.L. Arockiasamy, A. Nagendran, D. Mohan, Separation of proteins and toxic heavy metal ions from aqueous solution by CA/PC blend ultrafiltration membranes, Sep. Purif. Technol., 62 (2008) 32–38.

[16] A.M. Hidalgo, M. Gómez, M.D. Murcia, M. Serrano, R. Rodríguezschmidt, P.A. Escudero, Behaviour of polysulfone ultrafiltration membrane for dyes removal, Water Sci. Technol., 77 (2018) 2093–2100.

[17] F. Liu, N.A. Hashim, Y.T. Liu, M.R.M. Abed, K. Li, Progress in the production and modification of PVDF membranes, J. Membr. Sci., 375 (2011) 1–27.

[18] S. Munari, A. Bottino, G. Capannelli, Casting and performance of polyvinylidene fluoride based membranes, J. Membr. Sci., 16 (1983) 181–193.

[19] R. Pang, J. Li, K. Wei, X. Sun, J. Shen, W. Han, L. Wang, In situ preparation of Al-containing PVDF ultrafiltration membrane via sol-gel process, J. Colloid Interface Sci., 364 (2011) 373–378.

[20] Z. Fan, Z. Wang, M. Duan, J. Wang, S. Wang, Preparation and characterization of polyaniline/polysulfone nanocomposite ultrafiltration membrane, J. Membr. Sci., 310 (2008) 402–408.

[21] S. Liang, K. Xiao, Y. Mo, X. Huang, A novel ZnO nanoparticle blended polyvinylidene fluoride membrane for anti-irreversible fouling, J. Membr. Sci., 394–395 (2012) 184–192.

[22] A. Cui, Z. Liu, C. Xiao, Y. Zhang, Effect of micro-sized SiO_2-particle on the performance of PVDF blend membranes via TIPS, J. Membr. Sci., 360 (2010) 259–264.

[23] S. Iijima, Helical microtubules of graphitic carbon, Nature, 354 (1991) 56–58.

[24] L. Lu, H. Sun, F. Peng, Z. Jiang, Novel graphite-filled PVA/CS hybrid membrane for pervaporation of benzene/cyclohexane mixtures, J. Membr. Sci., 281 (2006) 245–252.

[25] V.K.K. Upadhyayula, S.G. Deng, M.C. Mitchell, G.B. Smith, Application of carbon nanotube technology for removal of contaminants in drinking water: a review, Sci. Total Environ., 408 (2009) 1–13.

[26] X. Peng, Z. Luan, J. Ding, Z. Di, Y. Li, B. Tian, Ceria nanoparticles supported on carbon nanotubes for the removal of arsenate from water, Mater. Lett., 59 (2005) 399–403.

[27] Z. Zhu, L. Wang, Y. Xu, Q. Li, J. Jiang, X. Wang, Preparation and characteristics of graphene oxide-blending PVDF nanohybrid membranes and their applications for hazardous dye adsorption and rejection, J. Colloid Interface Sci., 504 (2017) 429–439.

[28] D.A. Gopakumar, D. Pasquini, M.A. Henrique, L.C.D. Morais, Y. Grohens, S. Thomas, Meldrum's acid modified cellulose nanofiber-based polyvinylidene fluoride microfiltration membrane for dye water treatment and nanoparticle removal, ACS Sustain. Chem. Eng., 5 (2017) 2026–2033.

[29] L. Fan, C. Luo, M. Sun, X. Li, F. Lu, H. Qiu, Preparation of novel magnetic chitosan/graphene oxide composite as effective adsorbents toward methylene blue, Bioresour. Technol., 114 (2012) 703–706.

[30] J. Li, S. Zhang, C. Chen, G. Zhao, X. Yang, J. Li, X. Wang, Removal of Cu(II) and fulvic acid by graphene oxide nanosheets decorated with Fe_3O_4 nanoparticles, ACS Appl. Mater. Interfaces, 4 (2012) 4991–5000.

[31] D. Hou, Z. Wang, G. Li, H. Fan, J. Wang, H. Huang, Ultrasonic assisted direct contact membrane distillation hybrid process for membrane scaling mitigation, Desalination, 375 (2015) 33–39.

[32] L. Borea, V. Naddeo, M.S. Shalaby, T. Zarra, V. Belgiorno, H. Abdalla, A.M. Shaban, Wastewater treatment by membrane ultrafiltration enhanced with ultrasound: effect of membrane flux and ultrasonic frequency, Ultrasonics, 83 (2017) 42–47.

[33] M.M. Tao, F. Liu, L.X. Xue, Poly(vinylidene fluoride) membranes by an ultrasound assisted phase inversion method, Ultrason. Sonochem., 20 (2013) 232–238.

[34] G.J. Price, A. Fiona Keen, A.A. Clifton, Sonochemically-assisted modification of polyethylene surfaces, Macromolecules, 29 (1996) 5664–5670.

[35] S.J. Doktycz, K.S. Suslick, Interparticle collisions driven by ultrasound, Science, 247 (1990) 1067–1069.

[36] M. Nyström, M. Lindström, E. Matthiasson, Streaming potential as a tool in the characterization of ultrafiltration membranes, Colloids Surf., 36 (1989) 297–312.

[37] Z. Xu, J. Zhang, M. Shan, Y. Li, B. Li, J. Niu, B. Zhou, X. Qian, Organosilane-functionalized graphene oxide for enhanced antifouling and mechanical properties of polyvinylidene fluoride ultrafiltration membranes, J. Membr. Sci., 458 (2014) 1–13.

[38] R.C. Petersen, Interactions in the binary liquid system n,n-dimethylacetamide-water-viscosity and density, J. Phys. Chem., 64 (2002) 184–185.

[39] W.J. Bae, W.H. Jo, H.P. Yun, Preparation of polystyrene/polyaniline blends by in situ polymerization technique and their morphology and electrical property, Synth. Met., 132 (2003) 239–244.

[40] A.B. Albadarin, M.N. Collins, M. Naushad, S. Shirazian, G. Walker, C. Mangwandi, Activated lignin-chitosan extruded blends for efficient adsorption of methylene blue, Chem. Eng. J., 307 (2017) 264–272.

[41] E.I. El-Shafey, S.N.F. Ali, S. Al-Busafi, H.A.J. Al-Lawati, Preparation and characterization of surface functionalized activated carbons from date palm leaflets and application for methylene blue removal, J. Environ. Chem. Eng., 4 (2016) 2713–2724.

[42] J. Guo, S. Khan, S.-H. Cho, J. Kim, Preparation and immobilization of zinc sulfide (ZnS) nanoparticles on polyvinylidene fluoride pellets for photocatalytic degradation of methylene blue in wastewater, Appl. Surface Sci., 473 (2019) 425–432.

[43] T. Ahamad, M. Naushad, G.E. Eldesoky, S.I. Al-Saeedi, A. Nafady, N.S. Al-Kadhi, A.a.H. Al-Muhtaseb, A.A. Khan, A. Khan, Effective and fast adsorptive removal of toxic cationic dye (MB) from aqueous medium using amino-functionalized magnetic multiwall carbon nanotubes, J. Mol. Liq., 282 (2019) 154–161.

[44] Y.H. Li, S. Wang, Z. Luan, J. Ding, C. Xu, D. Wu, Adsorption of cadmium(II) from aqueous solution by surface oxidized carbon nanotubes, Carbon, 41 (2003) 1057–1062.

[45] X. Song, H. Liu, C. Lei, Y. Qu, Surface modification of coconut-based activated carbon by liquid-phase oxidation and its effects on lead ion adsorption, Desalination, 255 (2010) 78–83.

[46] B. Benguella, H. Benaissa, Cadmium removal from aqueous solutions by chitin: kinetic and equilibrium studies, Water Res., 36 (2002) 2463–2474.

[47] Y. Xie, C. He, L. Liu, L. Mao, K. Wang, Q. Huang, M. Liu, Q. Wan, F. Deng, H. Huang, Carbon nanotube based polymer nanocomposites: biomimic preparation and organic dye adsorption applications, RSC Adv., 5 (2015) 82503–82512.

[48] E. Daneshvar, A. Vazirzadeh, A. Niazi, M. Kousha, M. Naushad, A. Bhatnagar, Desorption of Methylene blue dye from brown macroalga: effects of operating parameters, isotherm study and kinetic modeling, J. Cleaner Prod., 152 (2017) 443–453.

[49] H. Deng, L. Yang, G. Tao, J. Dai, Preparation and characterization of activated carbon from cotton stalk by microwave assisted

chemical activation--application in methylene blue adsorption from aqueous solution, J. Hazard. Mater., 166 (2009) 1514–1521.

[50] Z.A. Al-Othman, R. Ali, M. Naushad, Hexavalent chromium removal from aqueous medium by activated carbon prepared from peanut shell: adsorption kinetics, equilibrium and thermodynamic studies, Chem. Eng. J., 184 (2012) 238–247.

[51] M. Naushad, Surfactant assisted nano-composite cation exchanger: development, characterization and applications for the removal of toxic Pb^{2+} from aqueous medium, Chem. Eng. J., 235 (2014) 100–108.

[52] M. Naushad, T. Ahamad, G. Sharma, A.a.H. Al-Muhtaseb, A.B. Albadarin, M.M. Alam, Z.A. Alothman, S.M. Alshehri, A.A. Ghfar, Synthesis and characterization of a new starch/SnO_2 nanocomposite for efficient adsorption of toxic Hg^{2+} metal ion, Chem. Eng. J., 300 (2016) 306–316.